

AperTO - Archivio Istituzionale Open Access dell'Università di Torino

Photocatalytic performances of rare earth element-doped zinc oxide toward pollutant abatement in water and wastewater

This is the author's manuscript

Original Citation:

Availability:

This version is available <http://hdl.handle.net/2318/1689456> since 2021-03-09T15:13:50Z

Published version:

DOI:10.1016/j.apcatb.2018.12.053

Terms of use:

Open Access

Anyone can freely access the full text of works made available as "Open Access". Works made available under a Creative Commons license can be used according to the terms and conditions of said license. Use of all other works requires consent of the right holder (author or publisher) if not exempted from copyright protection by the applicable law.

(Article begins on next page)

23

24 1. Introduction

25

26 Among semiconductor nanomaterials, ZnO has several interesting properties and broad applications.
27 Photocatalysts based on semiconductors are widely used in the conversion of light energy into useful
28 chemical energy. ZnO is considered as a benchmark catalyst due to its non-toxic nature coupled with low
29 cost [1]. One major drawback of existing technology is the low quantum efficiency of ZnO, which is due to
30 very fast recombination of photogenerated electron-hole pairs. In order to improve the photocatalytic
31 activity of ZnO, several modification methods have been developed. It has been reported that
32 photocatalytic performance of semiconductor photocatalyst can be improved by doping with certain
33 cations which can act as electron trapping agent to decrease the electron hole recombination rate [2, 3].

34 A possible way to improve the photocatalytic activity is the formation of semiconductor-semiconductor
35 p-n heterojunctions. It was found that the p-n junctions formed in combination with both p-type and n-
36 type semiconductors can effectively reduce the recombination rate of the photogenerated electron/hole
37 pairs, with consequent enhancement of the photocatalytic activity [4-7]. More recently, our and other
38 research groups started to investigate the role of rare earth elements (RE = La, Ce, Pr, Er and Yb) as dopant
39 of different oxides [8-10]. In a very recent paper we demonstrated that the presence in the mixed material
40 of CeO₂/ZnO interfaces appears responsible of specific photochemical properties [11]. The material is
41 composed of segregated CeO₂ nanoparticles supported on larger ZnO nanostructures. Nevertheless, the
42 presence of relatively low amounts of Ce (1%) were able to modify radically the behavior under irradiation.
43 This effect has been explained in terms of alignment of bands of the two different oxide phases respectively,
44 with the electron transfer from one species to the other helping the charge separation effect.

45 In previous papers [12, 13] we prepared pure and doped ZnO with low Ce loading (1% molar) *via*
46 hydrothermal process, a low temperature, green and simple process to obtain controlled nanostructures,
47 starting from different precursors. The specific percentage of 1% molar of dopant was chosen according to
48 the best photocatalytic results obtained. The photocatalytic activity of the synthesized materials was tested
49 on phenol [13] and on more refractory compounds, such as iodinated X-ray contrast agents (ICM) [2], which
50 are emerging contaminants, known to be scarcely abated in the wastewater treatment plants. Also in this
51 case the achievement of the fast drug disappearance was a great success. [13] The same material has been
52 successfully used in the abatement of acesulfame K, an artificial sweetener [12, 13].

53 Based on these very encouraging results, in a recent study we extended the investigation to other rare
54 earth elements (RE = La, Ce, Pr, Er and Yb). We synthesized *via* hydrothermal process and characterized
55 different photocatalysts based on ZnO doped with a low amount of RE (1% molar). [14-18]

56 In the present paper, we tested their photocatalytic performances toward a model pollutant, phenol, in
57 different matrices, namely MilliQ water and wastewater, to assess if the higher activity is still maintained
58 when facing with very complex and challenging matrices. Furthermore, through a comprehensive
59 electrochemical investigation and statistical analysis we were able to correlate the improved activity with
60 the different parameters affecting the photocatalytic process.

61

62 **2. Experimental section**

63 2.1. Materials

64 All reactants employed in this work were purchased from Aldrich with purity higher than 99.9% and were
65 used without any further purification treatment. Bare ZnO sample was synthesized starting from a 1 M
66 water solution of $\text{Zn}(\text{NO}_3)_2 \cdot 6\text{H}_2\text{O}$. Then a 4 M NaOH solution was added until the pH was 10-11, and finally
67 the solution was transferred into a PTFE lined stainless steel 100 mL autoclave (filling 70%), then treated at
68 175°C overnight. The product was centrifuged and washed with deionized water, then dried at 70°C. The
69 doped ZnO samples with rare earth elements RE 1% molar were prepared adding the stoichiometric
70 amount of RE chlorides in the starting solution, then the same procedure described in [14] has been
71 followed. The samples will be labelled as ZnO, ZnO-Ce, ZnO-La, ZnO-Yb, ZnO-Pr and ZnO-Er.

72 TiO_2 P25 Evonik was used as benchmark photocatalyst, after being irradiated and washed with ultrapure
73 water in order to eliminate the potential interference caused by adsorbed ions such as chloride, sulphate
74 and sodium.

75 Phenol (P), catechol (CAT), hydroquinone, methanol ($\geq 99.9\%$), acetonitrile ($\geq 99.9\%$) and formic acid(99%)
76 were purchased from Sigma Aldrich (Milan, Italy). HPLC grade water was obtained from MilliQ System
77 Academic (Waters, Millipore). HPLC grade methanol (BDH) and acetonitrile (Aldrich) were filtered through a
78 0.45 μm filter before use. Effluent and influent wastewaters (EWW and IWW, respectively) were provided
79 by ACEA Pinerolese (Italy, a standard treatment plant). Total organic carbon measured was 12.96 mg L^{-1} and
80 the pH was 8.05.

81

82 2.2. Materials characterization

83 SEM, TEM, XRD and BET DR-UV-Vis results were reported and deeply discussed in a previous paper. [14]
84 Here we remind that the specific surface area ($< 10 \text{ m}^2 \text{ g}^{-1}$) is very similar for all samples, as the UV-Vis
85 spectra, indicating that the RE insertion does not directly affect the VB \rightarrow CB transition. Nevertheless, in
86 the case of samples containing Pr, Er and Yb it is possible to detect the presence of a multitude of defined
87 absorption bands, related to the f-f transitions of Pr, Er and Yb ion states. The presence of these bands
88 indicates that the RE ions are well diluted in the matrix.

89
90
91
92
93
94
95
96
97
98
99
100
101
102
103
104
105
106
107
108
109
110
111
112
113
114
115
116
117
118
119
120
121

2.3. Photocatalytic tests

Irradiation experiments were carried out using air-saturated Pyrex glass cells filled with 5 mL of the solution of the target molecule. The concentration of phenol was 20 mg L⁻¹. The photocatalyst concentration was 1000 mg L⁻¹. Samples were irradiated using a Philips TLK/05 lamp 40 Watt with maximum emission at 365 nm. The incident irradiance was 25 W m⁻².

2.4. Analytical techniques

Phenol and its transformation products were monitored with a Merck-Hitachi liquid chromatograph equipped with Rheodyne injector L-6200 and L-6200A pumps for high-pressure gradients, L-4200 UV-Vis detector (the detection wavelength was set at 220 nm) and a LiChrocart RP-C18 column (Merck, 12,5 cm x 0,4 cm). Isocratic elution (1 mL min⁻¹ flow rate) was carried out with 80% of phosphate buffer 1x10⁻² M at pH 2.8 and 20% acetonitrile and retention times was 6.45 min.

2.5. Electrochemical tests

The electrochemical experiments were carried out with a standard photoelectrochemical set-up composed of a computer-controlled potentiostat, AUTOLAB PGSTAT12, and a 150 W LOT Oriel Xe arc lamp as radiation source. The incident irradiance on the sample was 84 W m⁻² in the 250-400 nm range. The electrochemical cell was a conventional three-electrode cell, in which the counter and reference electrodes were a Pt sheet and an Ag/AgCl/KCl 3 M electrode, respectively. If needed the electrolytic solution was purged with nitrogen or oxygen gas with purity 99.9999% obtained from Sapio (Italy). Transparent conductive supports (Corning® EXG alkaline earth boro-aluminosilicate glass, 25 x 25 x 1.1 mm, coated with Indium Tin Oxide on one surface, R_s = 9 - 15 Ω/□, Transmission >80%) were obtained from Delta Technologies Ltd (USA). In all cases electrolyte was KNO₃ 100 mM with K₂HPO₄ 10 mM at pH 8.85±0.05.

2.6. Electrode preparation

Working electrodes were prepared with doctor blade technique. The semiconductor powders were mixed with MilliQ® water to obtain slurries, and then deposited onto the conductive supports using adhesive tape as a spacer and a microscope slide to spread the slurry. In this way 20±5 mg of semiconductor were deposited on each electrode. Copper foil tape with conductive adhesive (RS Components, UK) was used to solder a copper wire and ensure the electric contact. The electric contact was insulated with black epoxy resin (RS Components, UK) to avoid its corrosion during electrochemical measurements. The area of the semiconductor coated surface was 2.25 cm².

122 3. Results

123 3.1. Photocatalytic test on phenol

124 The photocatalytic activity of pristine and rare earth elements doped ZnO-based materials was tested using
125 phenol as probe molecule. Adsorption experiments in the dark were performed in a 2 h time window and
126 showed that phenol was poorly adsorbed on all materials as adsorption was always below 10%. Direct
127 photolysis scarcely contributed to phenol transformation even after long irradiation times.

128 3.1.1. Tests in MilliQ water

129 The time evolution of phenol in MilliQ water in the presence of bare and rare earth elements doped ZnO
130 is reported in Figure 1. For comparison purpose, the degradation performed under the same conditions
131 with the benchmark TiO₂ P25 is shown as well. The degradation efficiency was very similar for P25 and bare
132 ZnO, while some difference arose for doped materials. Doping with lanthanum exhibited a slight
133 detrimental effect, while ZnO doped with cerium, erbium and ytterbium showed enhanced degradation
134 rates. The degradation curve approximated a pseudo-first-order kinetics and we calculated the kinetic
135 constants, which are collected in Figure 2. Excluding the case of cerium, the rate constant value seems
136 related to the number of electrons present in the f orbitals as the rate increases with increasing atomic
137 number Z. The diverse behavior of Ce-doped ZnO could be due to the different structure of this sample [14]
138 and, in particular, to the formation of two distinct phases, clearly observable in both XRD and TEM
139 measurements, which are not present with other doping elements.

140 Phenol transformation is known to occur through the formation of hydroxyl derivatives, i.e. catechol
141 (CAT), hydroquinone (HQ), 1,4-benzoquinone, resorcinol and, in a slight extent, of condensed products.[19]
142 In our experimental conditions, the intermediates were identified as HQ and CAT. In all cases, the time
143 evolution follows a typical bell-shaped profile, and differences arose from their net rate of formation-
144 disappearance when using TiO₂ and ZnO-based materials (Figure S1). In the case of P25, HQ was identified
145 at high amount (2.5 mg L⁻¹), while CAT was detected at very low concentration (0.2 mg L⁻¹), due to the
146 strong adsorption of catechol on the catalyst surface.[20, 21] This phenomenon was evidently less
147 important for ZnO based material as CAT and HQ were detected at comparable concentrations.

148 The maximum yield of CAT and HQ was reached with ZnO-Ce, ZnO-Er and ZnO-Yb in 15-20 min and then
149 almost 50% disappeared within 1 h of irradiation. The evolution rate was slowed down with ZnO, ZnO-La
150 and ZnO-Pr, the largest concentrations were achieved after 30 min and they did not significantly decrease
151 in the considered time window.

152

153 3.1.2. Tests in influent and effluent wastewaters

154 The time evolution for phenol in the presence of the catalysts in EWW and IWW are plotted in Figure 1,
155 together with the degradation profile obtained with the benchmark P25. In EWW, phenol was only partially
156 degraded with P25, while it was completely degraded with ZnO based materials. In particular, the
157 degradation was favored with ZnO-Yb and ZnO-Er. In IWW the rates were always slower than in EWW and
158 MilliQ water. The different performances of tested materials were even more marked with the following
159 order: ZnO-Yb, ZnO-Er > ZnO-Ce > ZnO-Pr > ZnO-La > ZnO. This trend, already observed in MilliQ water, seems
160 correlated to the atomic number, and then to the decrease of the ionic radius, with ZnO-Ce only
161 exception.[14]

162 The calculated kinetic constants in the different matrices are collected in Figure 2. It can be noted that all
163 zinc-based materials exhibited higher efficiency than P25. In MilliQ water, all synthesized materials except
164 ZnO-La were more efficient than P25 and, in particular, ZnO-Ce and ZnO-Yb were the most efficient at the
165 employed catalyst loading. [14] In the experiments performed in wastewater the performance of P25 was
166 deeply reduced, while ZnO-based materials were less influenced. Evidently, in the complex matrix typical of
167 a wastewater, there are species that like CAT, as observed before, can complex the surface and there act as
168 recombination centers, lowering the net photocatalytic activity.[22] Furthermore, both in EWW and in IWW
169 the catalyst efficiency increased with atomic number as in MilliQ water.

170 ZnO-Er and ZnO-Yb exhibited also the most efficient abatement of the transformation products (TPs). The
171 main TPs formed from phenol degradation were HQ and CAT and both materials were able to completely
172 abate them within 2h (EWW) or 4h (IWW) (see Figure S2 and S3 in Supplementary data, SD). As already
173 observed in MilliQ water, the concentration of CAT detected was very low with P25, due to the adsorption
174 on the catalyst surface, while with ZnO-based materials the two TPs are formed at similar amounts.
175 Considering EWW, the maximum yield of HQ and CAT was reached in 15 min with ZnO-Er and ZnO-Yb, while
176 longer times were required for the other materials. In the cases of P25, ZnO-La and ZnO-Pr, TPs were
177 accumulated and not completely degraded in the considered time window (Figure S2). In IWW, the
178 maximum amount of HQ and CAT was reached in 60 min with ZnO-Yb and ZnO-Er, while up to 120 min
179 were required for the other materials; in the case of ZnO-La, HQ did not reach the maximum in the
180 considered time (4h, see Figure S3).

181 **3.2. Electrochemical characterization**

182 All the recorded and calculated electrochemical data are reported in Table 1 and their significance is
183 explained in Table S1. The chronopotentiometry at open circuit potential (OCP) of undoped ZnO (Figure 3a)
184 revealed marked photoactivity as witnessed by the sudden decrease of the OCP under irradiation. The
185 measurements on other materials, which displayed similar trends, are reported in SD (Figures S4-S9). OCP
186 decreased until a steady state value under irradiation was reached (OCP2, Table 1). This value is a function

187 of the electrode characteristics and electrolyte composition. Indeed, when oxygen was bubbled in the
188 electrolyte instead of nitrogen, the OCP under irradiation stabilized to a significantly more positive value
189 (OCP5), whereas in the presence of methanol its value was more negative (OCP3 and OCP4). When
190 irradiation was interrupted, the OCP relaxed to the dark value over timescale of hundreds to thousands of
191 seconds, depending again on the working electrode material and electrolyte composition. The trends could
192 be replicated many times. We observed similar trends in the case of the doped ZnO specimens. For
193 reference, in the case of TiO₂ P25, the OCP values in deaerated electrolytes were significantly more
194 negative (Table 1). The OCP relaxation after irradiation with N₂ and O₂ purging, will be analyzed in the
195 following to estimate the recombination constant of the photogenerated charge carriers and the kinetic
196 constant for the reaction among photogenerated electrons and dissolved oxygen.

197 In cyclic voltammetry (CV) we observed a monotonic increase of the cathodic current density with
198 increasingly cathodic potential, and a cathodic current peak was never reached, as observed in previous
199 reports on semiconducting oxides.[23, 24] Conversely, we detected a marked anodic peak at -0.4 /-0.5 V
200 (depending on the scan rate) vs Ag/AgCl for both ZnO (Figure 3b) and doped ZnO specimens (see SD for
201 details). With O₂ purging the maximum current of the anodic peak was reduced for all the samples to less
202 than one half compared to deaerated electrolyte, whereas the cathodic current recorded at -1 V vs Ag/AgCl
203 increased compared to anoxic conditions, especially at lower scan rates (Figure 3c).

204 3.3. Discussion

205 The kinetic data reported in Figure 2 could be justified supposing that the rare earth-doping improves the
206 charge carrier separation. While this abused explanation could be possible in the case of Ce-doping, where
207 a biphasic system is present [11], it is harder to justify the better performance of the other specimens
208 where two different phases were not detected. For these reasons we checked the possibility of surface
209 adsorption of rare earth elements. As the proof that they are predominantly present at the surface is a
210 difficult task, we performed photocatalytic degradation experiments in the presence of fluorides, which
211 complex all these rare earth elements with almost the same stability constant ($\log\beta \approx 4$).[25] If the RE at
212 the surface played a significant role during the photocatalytic degradation, then their capping with fluoride
213 would affect the photocatalytic activity. The positive effect of fluoride on phenol photocatalytic
214 degradation on P25 was already reported. [22] The rate increase in the presence of fluoride was attributed
215 to the reduced adsorption of phenol degradation products, especially CAT, on P25 surface, thus limiting
216 substrate-mediated recombination. Here, in the presence of pristine ZnO no difference was observed (see
217 Figure S10), confirming the previous observation with CAT that ZnO surface is not prone to complexation.
218 Moreover, also in the presence of rare earth elements, except for La and Yb, no difference was observed
219 (see Figure S10), thus partially ruling out the hypothesis that the adsorption at the surface could play a

220 crucial role. For these reasons, we undertook a deep electrochemical study to possibly find the basic factors
221 influencing the observed rates.

222 Cyclic voltammetry is a tool to probe the density of states (DoS) of the electrode materials as a function of
223 the applied potential, and, therefore, to extract information about the redox potential of trap states, and of
224 the conduction and valence band of semiconducting electrodes. Indeed, when the potential is swept
225 toward negative values, the Fermi level in the semiconductor is displaced toward the conduction band,
226 while it is forced toward the valence band when the potential is swept in the positive direction. When the
227 applied potential forces the Fermi level inside the band-gap, the current density recorded is in the order of
228 $1 \mu\text{A cm}^{-2}$ or less, because the conductivity of the material is usually low, as it is the DoS at these potential
229 values. At energy levels close to the bands, the DoS usually increases exponentially because of the presence
230 of more trap states. The increase becomes more dramatic when the applied potential crosses the
231 conduction/valence band edges.[23] Nonetheless, it is not easy to determine the position of the band
232 edges by CV, because the band pinning regime cannot be guaranteed when trap states becomes charged,
233 i.e. exactly when the applied potential, and indeed the Fermi level, is about to reach the band edge, leading
234 to uncertainty in the exact determination of the band edge energy. On the other hand, the determination
235 of the trap state energy is more precise, especially in the case of deep traps, when the semiconductor is in
236 the band-pinning regime. If there are no redox couples in solution, the charge carriers promoted into the
237 semiconductor trap states due to the external bias cannot be transferred to the solution, and, especially if
238 the scan rate is high, trap states can reversibly be populated and depopulated, leading to reversible
239 voltammograms.[23] This is indeed the case of the CVs recorded under N_2 purging (Figures 3b and S4-S9
240 (b)), in which the anodic peak is clearly visible, whereas in the case of O_2 purging (Figure 3c and S4-S9 (c))
241 the marked reduction of the anodic current and the increased cathodic current witness that trapped
242 electrons in pristine and doped ZnO materials can reduce dissolved O_2 , in agreement with the results of the
243 photocatalytic tests. To confirm that the abatement of organic molecules obtained under irradiation is due
244 to the transfer of photogenerated charge carriers to solution species, and not to spurious effects, we
245 performed OCP measurements to assess the charge carrier reactivity.

246 OCP measurements can reveal photoactivity, discriminate between n-type and p-type semiconductors and,
247 eventually, if coupled to CV, quantify the photogenerated majority carrier density.[26] The photoactivity is
248 present in all the materials tested, as witnessed by the difference between dark potential and its value
249 upon irradiation (OCP1 and OCP2 in Table 1). Since in all cases the OCP equilibrated at significantly more
250 negative values compared to dark conditions, we concluded that ZnO and doped ZnO are n-type
251 semiconductors, and behave similarly to TiO_2 P25 (Figure 3a and Figures S4-S9 (a)). Indeed, in the case of n-
252 type semiconductors under irradiation, holes are trapped and transferred to solution species faster than
253 photoelectrons, which accumulate and shift the quasi Fermi level, and consequently the OCP, to more

254 negative potential. On the other hand, irradiating p-type semiconductors leads to hole accumulation and to
 255 a positive shift of the OCP. [24, 26] Steady state is achieved in approximately 1000-2000 s, because charge
 256 carriers generation and their loss reach the same rate when a certain photoelectron density n_{ph} is obtained.
 257 When electron and hole scavengers are not present in the electrolyte, charge carrier loss is mainly due to
 258 recombination. Therefore, in this case, when irradiation is interrupted, the OCP relaxation to its dark value
 259 gives information about the photoelectron recombination kinetics. To convert OCP values under irradiation
 260 and immediately after switching off the irradiation into photoelectron density n_{ph} , we integrated the
 261 cathodic current of the CV obtained at the fastest scan rate (200 mV s⁻¹), in order to ensure capacitive
 262 behavior, following Equation 1: [26]

$$n_{ph} = \frac{1}{e d A} \int_{E_{dark}}^{E_{light}} \frac{i}{s} dE$$

263 where e is the charge of the electron, d and A are the electrode thickness and area, respectively, i is the
 264 current recorded during the CV, s is the potential scan and E_{dark} and E_{light} are the OCP of the electrode
 265 recorded in the dark and under steady-state irradiation, respectively. The n_{ph} obtained under irradiation at
 266 steady state in deaerated (n_{ph2}) and in O₂-saturated electrolyte (n_{ph5}) are reported in Table 1. The OCP,
 267 which equilibrated at significantly more positive values in the presence of O₂; indicates that photoelectrons
 268 do not accumulate in these conditions, and demonstrates that all the materials can photo-reduce dissolved
 269 molecular oxygen. The values of n_{ph} under O₂ are lower compared to N₂ purging, usually by one order of
 270 magnitude. This evidence is coherent with CV results, where the intensity of the anodic current peak was
 271 significantly reduced in O₂ purged electrolyte.

272 The values of n_{ph} after light interruption were employed to compute recombination constants, k_R , in the
 273 case of deaerated electrolyte, where we assume that the main path to photoelectron decay is
 274 recombination with trapped holes. Conversely, we obtained kinetic constants for the reaction with
 275 dissolved O₂, k_{O_2} , in the case of O₂-saturated electrolyte, where photoelectrons are mainly lost because of
 276 the reduction reaction of O₂. Rate constants were evaluated assuming pseudo-first order kinetics [26]
 277 following the equation:

$$k_R = \frac{1}{n_{ph}} \frac{d n_{ph}}{dt}$$

278 Table 1 reports k_R and k_{O_2} values evaluated in two different conditions, i.e. at the corresponding OCP under
 279 irradiation ($k_{2,R}$ and k_{2,O_2}), and at an arbitrary photoelectron density of 10¹⁷ cm⁻³(k_R) and 10¹⁶ cm⁻³(k_{1,O_2}),
 280 respectively. This has been done because k_R and k_{O_2} are not necessarily constant as functions of n_{ph} and the
 281 OCP; because more negative OCP corresponds to larger photoelectron energy, and usually to increased

282 reactivity. This is the reason why k_R and k_{O_2} tend to increase with increasing n_{ph} and with increasingly
283 negative OCP values [26]. We ascribed the lack of anticorrelation between k_R and n_{ph} in deaerated
284 electrolytes to this effect. The OCP relaxation kinetics once irradiation is interrupted were significantly
285 faster in O_2 -purged electrolytes compared to deaerated solution for all the materials considered, as
286 witnessed by the difference between k_R and k_{O_2} , which is of two orders of magnitude for most of the
287 specimens, with the notable exception of ZnO-Er and TiO_2 P25, which appear to be the least reactive
288 materials with dissolved O_2 (k_{1,O_2} and k_{2,O_2} in Table 1). We can therefore conclude that photoelectron
289 reaction with dissolved O_2 is faster than recombination with trapped holes for all the materials here
290 presented, an essential feature for an efficient photocatalyst. This is even more pronounced in the case of
291 the ZnO specimens compared to TiO_2 P25.

292 Nevertheless, the above results are not sufficient to explain the photocatalytic activity in the degradation of
293 pollutants. The photocatalytic process is complex, and the overall rate is the result of the interplay among
294 several processes, (light absorption, generation, separation and reactivity) of the photogenerated charge-
295 carriers. Not all the factors can be estimated with the above-mentioned electrochemical measurements,
296 such as the role of crystalline facets exposed and the scattering and absorption efficiencies, and the
297 adsorption of substrates and reaction intermediates, although this last was ruled out before.[27-29]
298 However, the results of electrochemistry can help in decoupling some of these different factors, and in
299 particular the reactivity of charge carriers. With this aim we measured the perturbation of the OCP upon
300 the addition of different amounts of methanol.

301 After the addition of methanol, the OCP shifted to more negative values (OCP3 and OCP 4 in Table 1),
302 demonstrating that photogenerated holes are reactive towards organics such as methanol. Indeed, the hole
303 reaction with methanol reduced steady state concentration of holes and therefore also the photoelectron
304 recombination rate, which ultimately led to the OCP cathodic shift. This cathodic shift was proportional to
305 the methanol concentration in the electrolyte. Nevertheless, we detected a saturation effect of the
306 methanol concentration, especially for the undoped sample, for which we observed a cathodic shift of only
307 5 mV increasing methanol concentration from 60 to 600 mM. Owing to this saturation effect, and keeping
308 in mind that the most negative OCP reachable under irradiation is the E_{FB} , [30] we considered the OCP
309 under irradiation in the presence of 600 mM CH_3OH as an estimation of the E_{FB} for the materials under
310 investigation (E_{FB} in Table 1). This estimate is legitimate because the light intensity used was moderate (84
311 $W\ m^{-2}$ in the UV), electron scavengers were excluded (to favor photoelectron accumulation), recombination
312 rates were relatively low and further reduced upon the addition of a hole scavenger such as 600 mM
313 CH_3OH . Other procedures for E_{FB} estimation could not be employed in this case. Considering the porous
314 morphology of ZnO electrodes, their capacitance would not behave ideally, and therefore the Mott-
315 Schottky plots would deviate significantly from linearity,[24, 31] impeding the extraction of E_{FB} and donor

316 density with this strategy. Translating the E_{FB} obtained at pH 0 vs NHE (Table 1), we were able to compare
317 E_{FB} with water reduction potential. Since E_{FB} values obtained at pH 0 vs NHE were positive, we concluded
318 that ZnO and doped ZnO cannot promote photocatalytic water reduction and hydrogen production, as
319 opposed to TiO₂ P25. The E_{FB} values for ZnO materials were comprised between 92 and 262 mV vs NHE at
320 pH 0, showing an anticorrelation between E_{FB} and k_{2,O_2} ($r=0.70$) and k_{1,O_2} ($r=0.61$). We remember that the
321 critical value for the correlation constant r is $r = 0.608$ at 0.10 significance level for 4 degrees of freedom.
322 Being the correlations found larger than 0.608, the null hypothesis (no influence of E_{FB} on k_{O_2}) could be
323 discarded with 90% confidence. Four degrees of freedom were considered as the degrees of freedom are
324 the number of data couples minus two (in this case the six couples E_{FB} , k_{O_2}). The anticorrelation suggests
325 that the potential of the conduction band influences photoelectron transfer rate, and, therefore, if
326 photoelectron transfer were rate-limiting, E_{FB} might also play a role during the photocatalytic degradation
327 of organic compounds.

328 Another important piece of information was gathered taking into account the photocurrents recorded at
329 potentials 400 and 800 mV more positive than E_{FB} (I_{ph400} and I_{ph800} in Table 1). These potentials were
330 chosen to compare different semiconductors in the same conditions, because it is known that photocurrent
331 vanishes approaching E_{FB} . [30, 32] Moreover, comparing the photocurrents at two different potentials, we
332 were able to assess the effect of the external bias on photocurrent density. The photocurrents were anodic
333 for all the samples, confirming that the materials studied are n-type semiconductors. In this case ZnO-Er
334 presented the largest photocurrents, while the lowest values were recorded in the cases of undoped ZnO
335 and ZnO-Pr. Nevertheless, it is not possible to order unambiguously the materials with the photocurrent,
336 because the order is different as a function of the potential applied. There is a 3-fold increase in the case of
337 ZnO-La and ZnO-Er from $E_{FB} + 400$ mV to $E_{FB} + 800$ mV, whereas it is almost constant for TiO₂ P25 and ZnO-
338 Yb. Other cases are intermediate.

339 With the help of electrochemical tests we verified that for ZnO specimens the photocatalytic activity stems
340 from charge carrier separation upon irradiation and their reactivity with solution species (organics such as
341 methanol in the case of holes, and O₂ in the case of electrons). Nevertheless, from these data a complex
342 picture emerged, where there was not an electrochemical variable clearly responsible for the
343 photocatalytic rates observed. In these cases, considering two parameters at the time may result in
344 incomplete or misleading analysis of the results. For this reason, we undertook a partial least square (PLS)
345 analysis, in which the observed kinetic constants were expressed as functions of the electrochemical
346 parameters previously evaluated (Table 1). PLS is particularly suitable for this task, because it is not
347 adversely affected by collinear variables.

348 PLS analysis suggests that two PCs (principal components) are sufficient to predict the photocatalytic rates,
349 explaining 65 and 6% of the rate variance, respectively. From the analysis of the regression coefficients on

350 PC1 and PC2 we observed that all the experimental electrochemical variables contributed significantly to
351 PCs (Figure S11), with the exception of the OCP recorded in dark, which was not relevant for the
352 photodegradation experiments. Moreover, the absolute values of the regression coefficients were similar
353 for both PC1 and PC2. More pronounced differences in the regression coefficients of each parameter are
354 present in the case of PC2, as a function of the type of water used.

355 The observed rates (see Figure S12, reporting x and y loading weights) are strongly correlated to
356 photoelectron densities recorded in N₂ purged electrolyte (i.e. n_{ph2}, n_{ph3} and n_{ph4}, Table 1) and then are
357 linked to the absorption of the materials at $\lambda < 400$ nm. From the analysis of scores and loadings of the
358 electrochemical variables only (Figure 4) we infer that PC1 reflects n_{ph2}, n_{ph3} and n_{ph4}, i.e. the
359 photoelectron densities recorded in N₂ purged electrolyte with and without CH₃OH, while PC2 reflects n_{ph5}
360 and E_{FB}. ZnO-Yb displays a strong PC1 component. It is strongly correlated to n_{ph3} and n_{ph4}, thus suggesting
361 that Yb doping is beneficial for photoelectron accumulation.

362 The rates in MilliQ and waste water have very similar coordinates on PC1 and are only differentiated on
363 PC2. Because PC2 depends on E_{FB}, we conclude that larger reactivity on wastewater matrices is due to a
364 more positive E_{FB}, which implies a more positive valence band potential, and, therefore, more oxidizing
365 holes.

366 ZnO-Er lies at relatively high value of PC1 (as ZnO-Yb, see Figure 4) but at positive values of PC2. It is well
367 correlated to I_{ph800} (and I_{ph400}). Therefore, doping with Er promotes a positive E_{FB}, a large photocurrent
368 value, and, indeed, large photoelectron accumulation. Conversely, ZnO-Ce displays slightly positive
369 coordinate on PC1, markedly negative on PC2 (as ZnO-Yb), and strongly correlates with k_R and k_{1,02}. Ce
370 doping makes E_{FB} more negative, with a large increase in the charge transfer kinetics to dissolved oxygen. In
371 this case we can affirm that there is an improved charge carrier separation. The doping with La and Pr does
372 not significantly modify the performance compared with pristine ZnO. These specimens have negative
373 values of PC1, with null contribution from PC2. Compared with Ce, Er and Yb doping, these specimens have
374 lower photoelectron accumulation ability. Thus, PLS analysis effectively summarizes all the electrochemical
375 and photodegradation data and allows an interpretation of the role of each specific dopant: limited role for
376 La and Pr, improved photocurrent for Er, better accumulation of photoelectrons for Yb and faster electron
377 transfer for Ce.

378 4. Conclusions

379 Lanthanide-doped ZnO proved to be very effective in the degradation of pollutants, especially in real
380 wastewater matrices, where they outperformed the benchmark TiO₂ P25. Doping with Yb makes ZnO a
381 robust and efficient photocatalyst. The photoactivity probed with electrochemical techniques correlates
382 well with the photocatalytic activity in the degradation of model pollutants, also in matrices relevant for

383 real world application, especially when the photoelectron accumulation and charge carrier separation
384 properties are considered. Electrochemical evidences demonstrated how the photocatalytic activity stems
385 from a combination of different effects, often with opposite weight, i.e. the photoelectron density, the
386 conductivity of the interface (photocurrent, reactivity of electron with oxygen and of holes here
387 determined in the presence of methanol), and the recombination of charge carriers. When the combination
388 of these effects (absorption, catalytic and electronic) leads to positive results an improved electron-hole
389 separation effect is often loosely invoked. Conversely, the doping with rare earth elements affects
390 differently many important physical and chemical properties of ZnO such as: *i)* the light absorption
391 properties, which affect the photoelectron density and the photocurrent; *ii)* the recombination and O₂
392 reactivity constants; and, eventually, *iii)* the flat band potential, which determines the reactivity of the
393 photogenerated electrons.

394

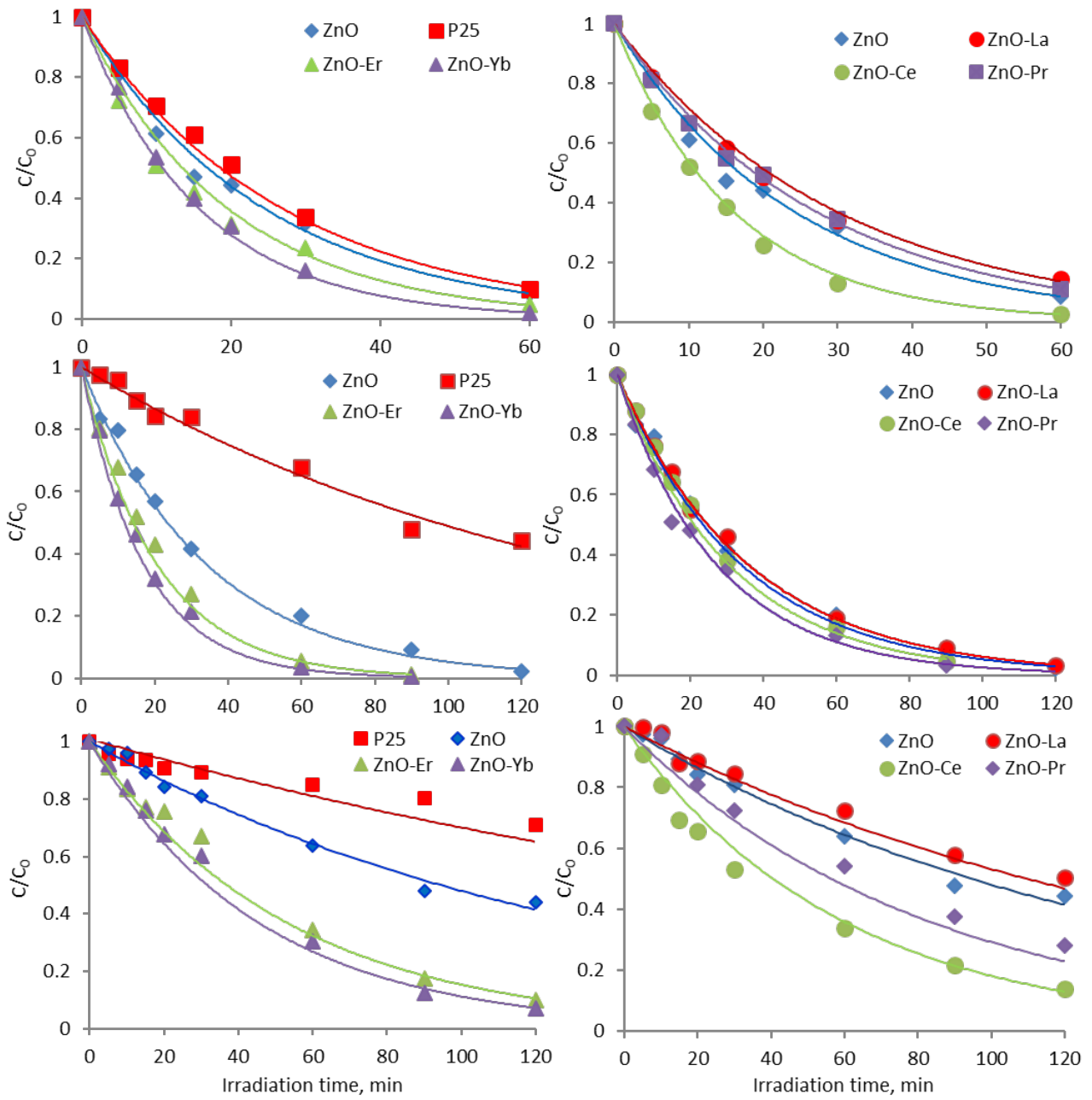
395 **Acknowledgments**

396 This Special Issue is dedicated to honor the retirement of Prof. César Pulgarin at the Swiss Federal Institute
397 of Technology (EPFL, Switzerland), a key Figure in the area of Catalytic Advanced Oxidation Processes. We
398 also acknowledge support by MIUR, in the frame of the international consortium WATERJPI2013-MOTREM
399 of the "Water Challenges for a Changing World" Joint Programming Initiative (WaterJPI) Pilot Call and ACEA
400 Pinerolese for providing water samples.

401

402 **Figures**

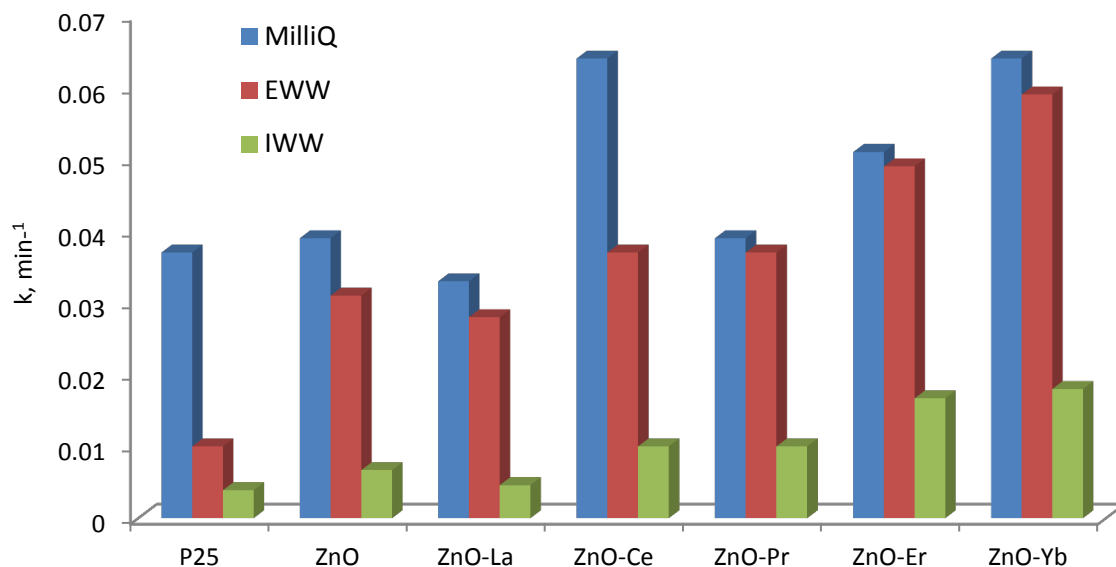
403



404

405 **Figure 1.** Phenol degradation curves in the presence of different catalysts under UV-A light in MilliQ water
406 (top), EWW (middle) and IWW (bottom).

407

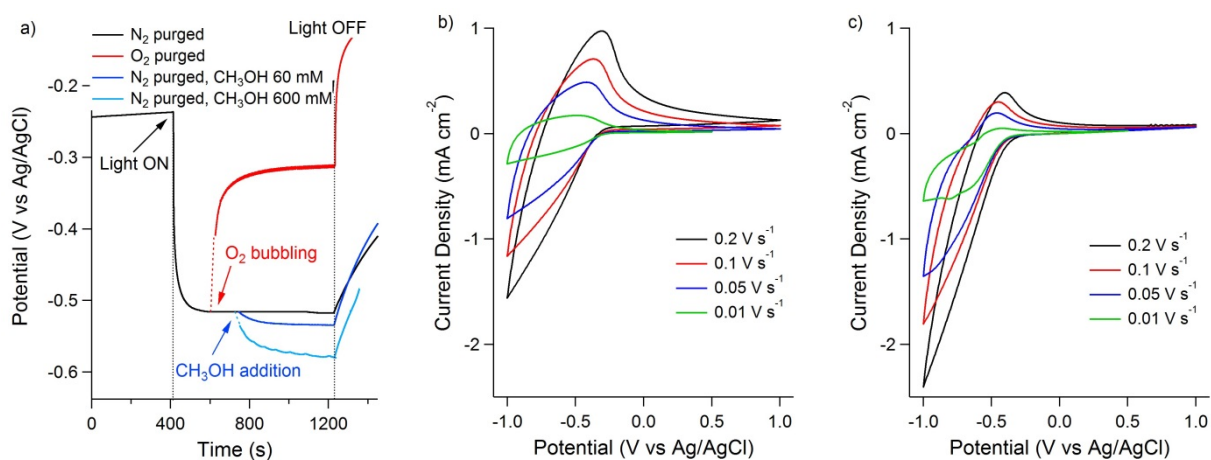


408

409 **Figure 2.** Kinetic constants (k) calculated in ultrapure water (■), EWW (■) and IWW (■). Numerical data are
 410 reported in Table 1.

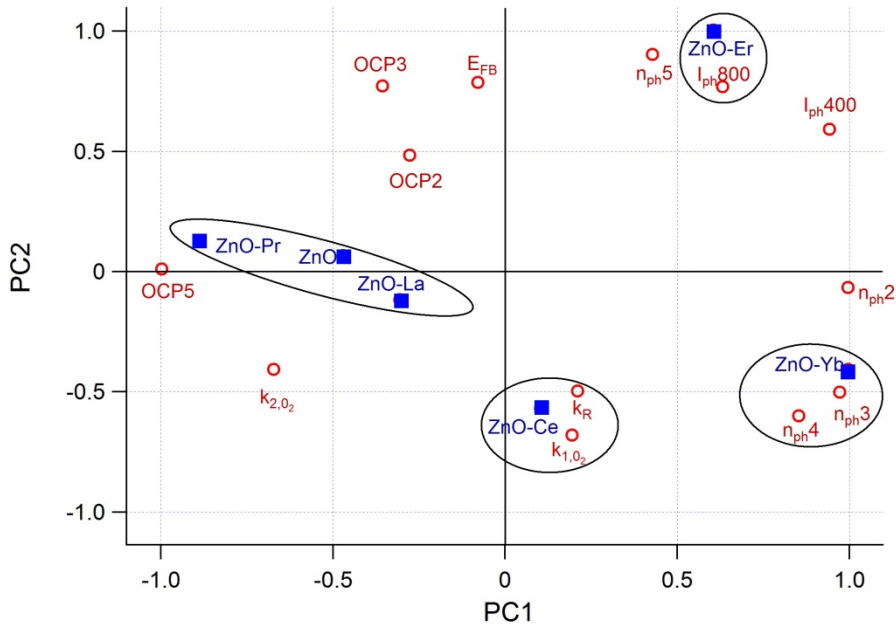
411

412



413

414 **Figure 3.** Chronopotentiometries under different conditions (a) and cyclic voltammeteries at different
 415 potential scan rates of ZnO in N₂ (b) and O₂ (c) purged electrolytes.



416

417 **Figure 4.** Score and loading weights of the electrochemical variables in the PC plane. PC1 and PC2 explain
 418 65 and 6% of variance, respectively. Circles gather together correlated variables and samples, as presented
 419 in the discussion section.

420

421 **Table 1.** Open circuit potential values (vs Ag/AgCl, unless otherwise stated) in different electrolytes and
 422 photocurrent values obtained from CV under N₂ purge at scan rate 10 mV s⁻¹; photoelectron densities (cm⁻³)
 423 in different electrolytes and rate constants (s⁻¹) for recombination and reaction with O₂ for P25, pristine and
 424 doped ZnO; the last 3 rows report the first order degradation constants for phenol, already plotted in
 425 Figure 2.

Acronym	Conditions	ZnO	ZnO-La	ZnO-Ce	ZnO-Pr	ZnO-Er	ZnO-Yb	TiO ₂ P25
OCP1	Dark, N ₂ purged, mV	-9.5	-172	-103.2	173	-9.5	-190.5	-67
OCP2	Light, N ₂ purged (OCP _{N₂, light}), mV	-515.0	-444.7	-441.2	-452.7	-415.6	-545.3	-773.4
OCP3	Light, N ₂ purged, CH ₃ OH 60 mM, mV	-529.8	-505.5	-513.0	-480.2	-436.6	-589.8	-875.9
OCP4	Light, N ₂ purged, CH ₃ OH 600 mM (E _{FB} pH 8.85), mV	-579.8	-565.1	-542.5	-529.8	-454.6	-624.5	-922.6
OCP5	Light, O ₂ purged, (OCP _{O₂, light}), mV	-314.4	-273	-269.6	-167.0	-320	-361	-122
I _{ph400}	Photocurrent at E _{FB} + 400 mV, μA	8±1	8±2	15±1	8±1	35±5	20±1	15±2
I _{ph800}	Photocurrent at E _{FB} + 800 mV, μA	15±2	25±5	25±2	11±1	85±5	21±2	15±1
E _{FB}	E _{FB} pH 0 vs NHE, mV	139.9	154.1	176.7	176.4	262.2	92.3	-200.5
n _{ph2}	Light, N ₂ purged, cm ⁻³	1.4·10 ¹⁷	2.0·10 ¹⁷	1.3·10 ¹⁷	1.2·10 ¹⁷	2.0·10 ¹⁷	3.1·10 ¹⁷	0.4·10 ¹⁷
n _{ph3}	Light, N ₂ purged, CH ₃ OH 60 mM, cm ⁻³	1.6·10 ¹⁷	2.8·10 ¹⁷	3.1·10 ¹⁷	1.5·10 ¹⁷	2.2·10 ¹⁷	4.7·10 ¹⁷	1.5·10 ¹⁷
n _{ph4}	Light, N ₂ purged, CH ₃ OH 600 mM (E _{FB} pH 8.85), cm ⁻³	1.9·10 ¹⁷	3.9·10 ¹⁷	4.2·10 ¹⁷	2.0·10 ¹⁷	2.4·10 ¹⁷	6.1·10 ¹⁷	2.7·10 ¹⁷
n _{ph5}	Light, O ₂ purged, cm ⁻³	4.5·10 ¹⁶	2.5·10 ¹⁶	1.0·10 ¹⁶	1.4·10 ¹⁶	12.5·10 ¹⁶	1.9·10 ¹⁶	0.1·10 ¹⁶
k _R	k _R @ 1.0·10 ¹⁷ cm ⁻³ , s ⁻¹	2.5·10 ⁻³	1.1·10 ⁻³	35·10 ⁻³ (extr)	0.8·10 ⁻³	2.8·10 ⁻³	5.0·10 ⁻³	4·10 ⁻³ (a)
K _{2,R}	k _R @ OCP _{N₂, light} , s ⁻¹	3.2·10 ⁻³	2.6·10 ⁻³	10.0·10 ⁻³	2.5·10 ⁻³	6.1·10 ⁻³	3.7·10 ⁻³	2.5·10 ⁻³
K _{1,O2}	k _{O2} @ 1.0·10 ¹⁶ cm ⁻³ , s ⁻¹	0.03	0.17	0.10	0.04	0.001	0.13	0.15(a)
K _{2,O2}	k _{O2} @ OCP _{O₂, light} , s ⁻¹	0.25	0.27	0.10	0.20	0.03	0.18	0.02
k _W	In MilliQ water, min ⁻¹	0.039	0.033	0.064	0.039	0.051	0.064	0.037
k _E	In EWW, min ⁻¹	0.031	0.028	0.037	0.037	0.049	0.059	0.01
k _I	In IWW, min ⁻¹	0.0067	0.0046	0.01	0.01	0.0167	0.018	0.0039

426 a) extrapolated

427

- 429 [1] A.A. Ismail, A. El-Midany, E.A. Abdel-Aal, H. El-Shall, Application of statistical design to optimize the preparation of
430 ZnO nanoparticles via hydrothermal technique, *Mater. Lett.* 59 (2005) 1924-1928.
- 431 [2] W. Zhang, Z. Zhong, Y. Wang, R. Xu, Doped solid solution: $(\text{Zn}_{0.95}\text{Cu}_{0.05})_{1-x}\text{Cd}_x\text{S}$ nanocrystals with high activity for H_2
432 evolution from aqueous solutions under visible light, *J. Phys. Chem. C* 112 (2008) 17635-17642.
- 433 [3] R. Kumar, A. Umar, G. Kumar, M.S. Akhtar, Y. Wang, S.H. Kim, Ce-doped ZnO nanoparticles for efficient
434 photocatalytic degradation of direct red-23 dye, *Ceram. Int.* 41 (2015) 7773-7782.
- 435 [4] D. Sarkar, C.K. Ghosh, S. Mukherjee, K.K. Chattopadhyay, Three dimensional $\text{Ag}_2\text{O}/\text{TiO}_2$ type-II (p-n)
436 nanoheterojunctions for superior photocatalytic activity, *ACS Appl. Mat. Interfaces* 5 (2012) 331-337.
- 437 [5] M. Li, W. Wu, K. Liu, G. Hu, H. Xu, Three-dimensional assembly and electrical properties of $\text{Cu}_2\text{O}/\text{ZnO}$
438 heterojunction via an electrochemical superfilling method, *Electrochim. Acta* 71 (2012) 100-105.
- 439 [6] L. Ma, H. Fan, H. Tian, J. Fang, X. Qian, The n-ZnO/n- In_2O_3 heterojunction formed by a surface-modification and
440 their potential barrier-control in methanal gas sensing, *Sensors and Actuators B: Chemical* 222 (2016) 508-516.
- 441 [7] G. Mohamed Reda, H. Fan, H. Tian, Room-temperature solid state synthesis of $\text{Co}_3\text{O}_4/\text{ZnO}$ p-n heterostructure and
442 its photocatalytic activity, *Adv. Powder Technol.* 28 (2017) 953-963.
- 443 [8] C. Gionco, M.C. Paganini, E. Giamello, R. Burgess, C. Di Valentin, G. Pacchioni, Cerium-Doped Zirconium Dioxide, a
444 Visible-Light-Sensitive Photoactive Material of Third Generation, *J. Phys. Chem. Lett.* 5 (2014) 447-451.
- 445 [9] C. Jayachandriah, G. Krishnaiah, Influence of cerium dopant on magnetic and dielectric properties of ZnO
446 nanoparticles, *J. Mater. Sci.* 52 (2017) 7058-7066.
- 447 [10] O. Bechambi, A. Touati, S. Sayadi, W. Najjar, Effect of cerium doping on the textural, structural and optical
448 properties of zinc oxide: Role of cerium and hydrogen peroxide to enhance the photocatalytic degradation of
449 endocrine disrupting compounds, *Mater. Sci. Semicond. Process.* 39 (2015) 807-816.
- 450 [11] E. Cerrato, C. Gionco, M.C. Paganini, E. Giamello, E. Albanese, G. Pacchioni, Origin of Visible Light Photoactivity of
451 the CeO_2/ZnO Heterojunction, *ACS Applied Energy Materials* 1 (2018) 4247-4260.
- 452 [12] P. Calza, C. Gionco, M. Giletta, M. Kalaboka, V.A. Sakkas, T. Albanis, M.C. Paganini, Assessment of the abatement
453 of acelsulfame K using cerium doped ZnO as photocatalyst, *J. Hazard. Mater.* 323 (2016) 471-477.
- 454 [13] M.C. Paganini, D. Dalmasso, C. Gionco, V. Polliotto, L. Mantilleri, P. Calza, Beyond TiO_2 : Cerium-Doped Zinc Oxide
455 as a New Photocatalyst for the Photodegradation of Persistent Pollutants, *ChemistrySelect* 1 (2016) 3377-3383.
- 456 [14] E. Cerrato, C. Gionco, I. Berruti, F. Sordello, P. Calza, M.C. Paganini, Rare earth ions doped ZnO: Synthesis,
457 characterization and preliminary photoactivity assessment, *J. Solid State Chem.* 264 (2018) 42-47.
- 458 [15] N. Yao, J. Huang, K. Fu, S. Liu, E. Dong, Y. Wang, X. Xu, M. Zhu, B. Cao, Efficiency enhancement in dye-sensitized
459 solar cells with down conversion material ZnO: Eu^{3+} , Dy^{3+} , *J. Power Sources* 267 (2014) 405-410.
- 460 [16] M. Faisal, A.A. Ismail, A.A. Ibrahim, H. Bouzid, S.A. Al-Sayari, Highly efficient photocatalyst based on Ce doped ZnO
461 nanorods: Controllable synthesis and enhanced photocatalytic activity, *Chem. Eng. J.* 229 (2013) 225-233.
- 462 [17] P.V. Korake, R.S. Dhabbe, A.N. Kadam, Y.B. Gaikwad, K.M. Garadkar, Highly active lanthanum doped ZnO
463 nanorods for photodegradation of metasytox, *J. Photochem. Photobiol. B Biol.* 130 (2014) 11-19.
- 464 [18] A.S. Weber, A.M. Grady, R.T. Koodali, Lanthanide modified semiconductor photocatalysts, *Catal. Sci. Technol.* 2
465 (2012) 683-693.
- 466 [19] V. Augugliaro, L. Palmisano, A. Sclafani, C. Minero, E. Pelizzetti, Photocatalytic degradation of phenol in aqueous
467 titanium dioxide dispersions, *Toxicol. Environ. Chem.* 16 (1988) 89-109.
- 468 [20] P.A. Connor, K.D. Dobson, A.J. McQuillan, New Sol-Gel Attenuated Total Reflection Infrared Spectroscopic Method
469 for Analysis of Adsorption at Metal Oxide Surfaces in Aqueous Solutions. Chelation of TiO_2 , ZrO_2 , and Al_2O_3 Surfaces by
470 Catechol, 8-Quinolinol, and Acetylacetone, *Langmuir* 11 (1995) 4193-4195.
- 471 [21] X.J. Li, J.W. Cabbage, W.S. Jenks, Photocatalytic degradation of 4-chlorophenol. 2. The 4-chlorocatechol pathway,
472 *J. Org. Chem.* 64 (1999) 8525-8536.
- 473 [22] C. Minero, G. Mariella, V. Maurino, E. Pelizzetti, Photocatalytic Transformation of Organic Compounds in the
474 Presence of Inorganic Anions. 1. Hydroxyl-Mediated and Direct Electron-Transfer Reactions of Phenol on a Titanium
475 Dioxide-Fluoride System, *Langmuir* 16 (2000) 2632-2641.
- 476 [23] F. Fabregat-Santiago, I. Mora-Sero, G. Garcia-Belmonte, J. Bisquert, Cyclic voltammetry studies of nanoporous
477 semiconductors. Capacitive and reactive properties of nanocrystalline TiO_2 electrodes in aqueous electrolyte, *J. Phys.*
478 *Chem. B* 107 (2003) 758-768.
- 479 [24] F. Sordello, V. Maurino, C. Minero, Photoelectrochemical study of TiO_2 inverse opals, *J. Mater. Chem.* 21 (2011)
480 19144 - 19152.
- 481 [25] Y.-R. Luo, R.H. Byrne, The Influence of Ionic Strength on Yttrium and Rare Earth Element Complexation by Fluoride
482 Ions in NaClO_4 , NaNO_3 and NaCl Solutions at 25 °C, *Journal of Solution Chemistry* 36 (2007) 673.

- 483 [26] D. Monllor-Satoca, R. Gomez, Electrochemical Method for Studying the Kinetics of Electron Recombination and
484 Transfer Reactions in Heterogeneous Photocatalysis: The Effect of Fluorination on TiO₂ Nanoporous Layers, J. Phys.
485 Chem. C 112 (2007) 139-147.
- 486 [27] C. Minero, D. Vione, A quantitative evaluation of the photocatalytic performance of TiO₂ slurries, Appl. Catal. B:
487 Environ. 67 (2006) 257-269.
- 488 [28] T. Ohno, K. Sarukawa, M. Matsumura, Crystal faces of rutile and anatase TiO₂ particles and their roles in
489 photocatalytic reactions, New J. Chem. 26 (2002) 1167-1170.
- 490 [29] F. Pellegrino, L. Pellutiè, F. Sordello, C. Minero, E. Ortel, V.-D. Hodoroaba, V. Maurino, Influence of agglomeration
491 and aggregation on the photocatalytic activity of TiO₂ nanoparticles, Appl. Catal. B: Environ. 216 (2017) 80-87.
- 492 [30] R. Beranek, (Photo)electrochemical Methods for the Determination of the Band Edge Positions of TiO₂-Based
493 Nanomaterials, Advances in Physical Chemistry 2011 (2011) 786759.
- 494 [31] B.H. Ernè, D. Vanmaekelbergh, J.J. Kelly, Morphology and strongly enhanced photoresponse of GaP electrodes
495 made porous by anodic etching, J. Electrochem. Soc. 143 (1996) 305-314.
- 496 [32] M.A. Alpuche-Aviles, Y. Wu, Photoelectrochemical Study of the Band Structure of Zn₂SnO₄ Prepared by the
497 Hydrothermal Method, J. Am. Chem. Soc. 131 (2009) 3216-3224.